A Computational Research on Ag(I)-Catalyzed Cubane Rearrangement: Mechanism, Metal and Counteranion Effect, Ligand Engineering and Post-Transition State Desymmetrization

Yumiao Ma*[a,b]
[a] BSJ Institute, Haidian, Beijing, People's Republic of China, 100084, ymma@bsj-institute.top.
[b] Hangzhou Yanqu Information Technology Co., Ltd., Xihu District, Hangzhou City, Zhejiang Province, 310003, People's Republic of China.

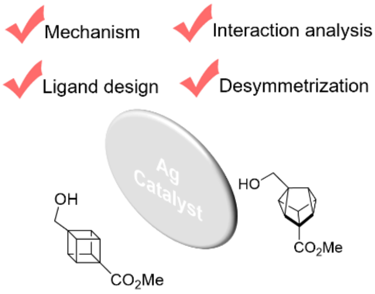

Abstract

Ag(I) salts have demonstrated superior catalytic activity in the cubane-cuneane rearrangement. This research presents a comprehensive mechanistic investigation to answer the following questions: (1) What is the specific mechanism involved? (2) How does Ag differ from other metals in this context? (3) What is the nature of the oxidative addition by Ag(I) salts? (4) How does the choice of ligand or counteranion influence the reaction? Based on the mechanistic findings, a catalytic system based on a chiral ether ligand is predicted to exhibit milder Lewis acidity, lower reaction barriers, higher chemoselectivity, and the potential for achieving enantioselective synthesis through post-transition state desymmetrization.

Introduction

Transition metal-catalyzed chemical transformations form a solid foundation of modern chemistry. Among the transition metals, the d-block noble metals[1-2]—Pd[3-4], Ru[5-6], Rh[7], and Ir[8]—have been extensively studied and applied. Additionally, the catalytic application of other d-block metals such as Mn[9], Fe[10-11], Co[12], and Ni[13-14] has rapidly emerged. As for the ds-block elements, Cu[15-18] and Au[19-20] have also been extensively explored. However, the catalytic behavior of Ag in organometallic compounds remains relatively unexplored[21-26], creating an intriguing knowledge gap. In recent years, cuneanes, a class of caged polycyclic hydrocarbons, have garnered interest due to their unique skeleton structure, which enables their applications in liquid crystal technology and as bioisosteres of benzene in medicinal development. The skeletal rearrangement of cubanes to cuneanes, catalyzed by Ag(I) catalysts, was first reported by Eaton in 1970[27]. Although Au(I) and certain intricately designed Pd(II) complexes have also been employed[28], Ag(I) catalysts display superior activity, providing an ideal platform to study the behavior of Ag in organometallic chemistry. When a 1,6-disubstituted cubane is used as the substrate, two products—**Prod1** and **Prod2**—can be generated depending on the metal, ligand, and counteranion employed. In 2023, Lam[29], Nagasawa[30] and Stephenson[31] reported new progress on this reaction nearly at the same time. In Lam's report, a mild strategy using $AgNTf_2$ as the catalyst, selectively yielding **Prod1** at room temperature with dichloromethane (DCM) as the solvent (Figure 1). Despite the advantages of Lam's reaction, the reaction is incompatible with functional groups such as tertiary alcohols and Troc-protected amino groups, possibly due to the Lewis acidity of the Ag(I) catalyst. To comprehend the selectivity, enhance catalytic activity, and broaden the substrate scope, a thorough understanding of the mechanism is necessary.

The rearrangement is proposed to occur through a mechanism involving oxidative addition (OA) to the C–C σ-bond, heterolytic cleavage of the metal–carbon bond, and subsequent tandem carbocation rearrangement (Figure 1). In this study, we investigate the mechanism using density functional theory (DFT), high-level coupled cluster (DLPNO-CCSD(T)), and quasi-classical molecular dynamics calculations to address the following questions: (1) What is the actual mechanism, and which step determines the selectivity? (2) What is the nature of the OA step into a strained C–C bond? (3) Why do Ag(I) catalysts exhibit superior reactivity, and how do they differ from other metals during the OA step? (4) How can we further enhance Lam's reaction? (5) Is it possible to achieve enantioselective synthesis of the cuneane product from an achiral 1,6-disubstituted substrate?

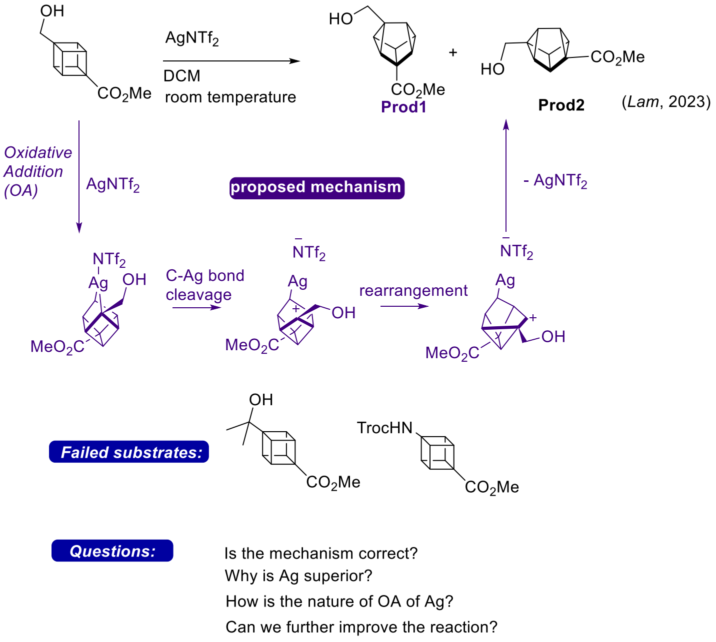

Figure 1. A summary of Lam’s report and the questions to be investigated in this research.

Methods

All calculations were performed using Gaussian 16 program[32]. For geometry optimization, the PBE0 functional[33] was used with the SDD pseudopotential basis set for metals and 6-31+G(d,p) basis set[34-39] for other atoms, in combination with the with Grimme’s D3BJ dispersion correction[40] and SMD implicit solvation model[41] using dichloromethane as the solvent. All minimums and transition states were verified by frequency calculation, and thermal corrections at 298.15 K were obtained at the same level. Single point energies were calculated at DLPNO-CCSD(T)/def2-TZVPPD level[42-44] using the ORCA program[45]. According to Coote *et al.*’s recommendation[46], the solvation free energy of each compound was obtained at M05-2X/6-31G(d) level[47], while SDD was used for metals. The final Gibbs free energy of each compound is obtained by the following method: G = thermal correction (PBE0-D3BJ/6-31+G(d,p)/SDD/SMD) + E(M05-2X/6-31G(d)/SDD/SMD) – E(M05-2X/6-31G(d)/SDD/gas) + E(DLPNO-CCSD(T)/def2-TZVPPD) + 1.89 kcal/mol

Optimized structures were illustrated using CYLview[48]. The orbital isosurface data were derived using Multiwfn and visualized by VMD[49].

The quasi-classical trajectory molecular dynamics simulations were performed using the

PROGDYN program[50]. The initial geometry for each trajectory was generated by adding displacements that follow a QM-like Gaussian distribution to all vibrational modes higher than 10 cm^{-1} of the initial geometry. Each real normal mode was given its zero-point energy plus a random Boltzmann sampling of the thermal energy available at 298.15 K. Trajectories were propagated at the same theoretical level as geometry optimization in both the forward and backward directions, until the product forms or the length of trajectory is longer than 2000 fs.

Results and Discussion

Mechanism: The mechanism of Lam's reaction was initially investigated within the previously accepted mechanistic framework. The coordination of $AgNTf_2$ to the cubane substrate **1** is exothermic, releasing -8.3 kcal/mol of energy and forming the Ag–O complex **Int1**. Subsequently, an OA into one of the C–C bonds occurs. Among the three groups of equivalent C–C bonds (labelled as purple for C1–C2, orange for C2–C3, and blue for C3–C6 in Figure 2), the previously proposed mechanism suggests OA into the C1–C2 bond. However, high-level computational results suggest that the OA into the C2–C3 bond exhibits the lowest barrier (14.7 kcal/mol through **TS1c**), while the OA into the C1–C2 and C3–C6 bonds requires barriers of 17.1 kcal/mol (through **TS1a**) and 19.5 kcal/mol (through **TS1b**), respectively. The Ag(III) complex, **Int2a**, **Int2b**, and **Int2c**, exhibit similar free energies (0.7 ~ 2.1 kcal/mol).

Subsequently, one of the Ag–C bonds undergoes heterolytic cleavage, enabling a carbocation rearrangement. Both **Int2a** and **Int2c** favor the cleavage of the Ag–C bond close to the CH_2OH substituent group (through **TS2a** and **TS2c**, respectively), likely due to its stabilization of the developing carbocation. In the case of **Int2a**, the cleavage of the Ag–C bond through **TS2a** leads to the formation of a carbocation intermediate, **Int3a**. Although a transition state (TS) exists for the subsequent rearrangement on the electronic energy surface, its free energy is lower than that of **Int3a**, suggesting that the rearrangement is almost barrierless. In **Int2c**, the cleavage of the Ag–C bond through **TS2c** enables a concerted rearrangement that directly leads to the final product (the concertedness and dynamic behavior of this step will be discussed later). Both pathways through **TS2a** and **TS2c** result in the formation of **Prod1**.

The formation of **Prod2** occurs through the cleavage of the Ag–C bond near the CO_2Me group via **TS2a'** or **TS2c'**, which requires a higher energy barrier. Considering that the energy of **TS1b** is significantly higher than that of all the other TSs except **TS2a'**, it is expected that the reaction pathway through C3–C6 oxidative addition plays a minor role. Therefore, further exploration of the subsequent transformations was not conducted.

The energies of **TS1**s and **TS2**s are quite similar. As a result, the reaction does not have a single rate-determining step. The overall barrier for forming **Prod1** through OA into C1–C2 and C2–C3 bond is 17.1 kcal/mol (determined by **TS1a**) and 16.3 kcal/mol (determined by **TS2c**), respectively. The small difference in barriers suggests that both pathways coexist, although the latter contributes more. The overall barrier to forming **Prod2** is 17.7 kcal/mol, as determined by **TS2c'**. The computational results suggest that **Prod1** is favored by ~1.4 kcal/mol, suggesting a **Prod1**/**Prod2** ratio of 13:1, which is roughly consistent with the experimental observation of 25:1.

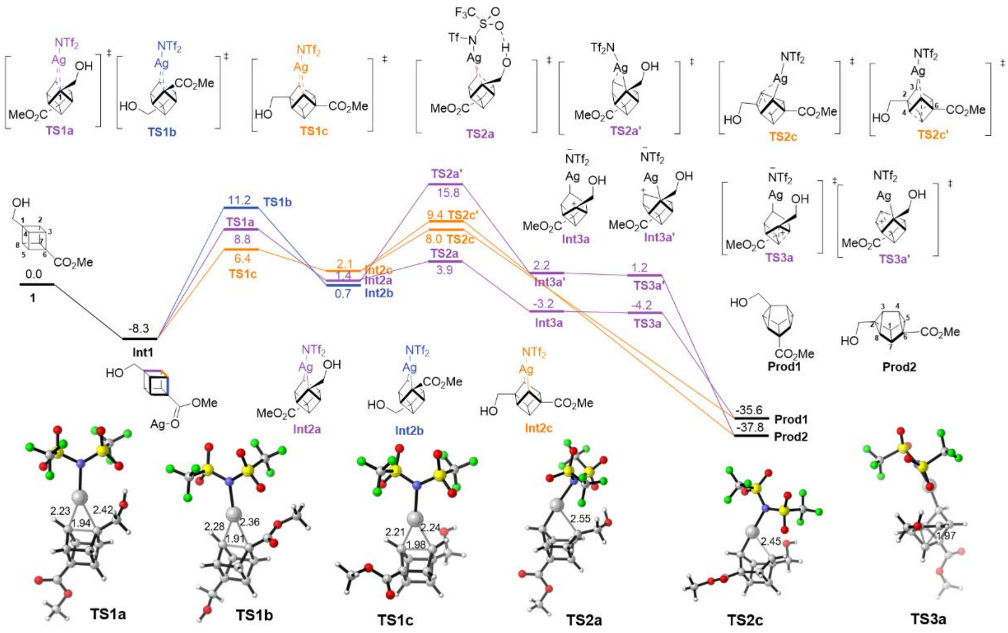

Figure 2. Gibbs free energy profile (kcal/mol) of the cubane rearrangement catalyzed by AgNTf$_2$, as well as the geometries of selected key species. The bond lengths are in angstrom.

Overall, the DFT and DLPNO-CCSD(T) calculations in this section indicate that the reaction follows an oxidative addition-Ag–C bond cleavage-carbocation rearrangement mechanism. However, contrary to the previously proposed C1–C2 oxidative addition, the AgNTf$_2$ catalyst exhibits a preference for oxidative addition into the C2–C3 bond. Both pathways contribute to the formation of the observed products, **Prod1** and **Prod2**, depending on which of the two Ag–C bonds undergoes heterolytic cleavage. The overall barrier is determined by both the oxidative addition and the Ag–C bond cleavage steps, with computations suggesting a preference for the formation of **Prod1**.

Nature of the rearrangement process: According to the preceding discussion, the formation of the observed product can be attributed to four processes, as illustrated in Figure 3. Each of these processes involves three stages of bond cleavage and formation. Initially, one of the C–Ag bonds undergoes heterolytic cleavage, generating a cyclobutyl carbocation. Subsequently, a neighboring C–C bond migrates towards the carbocation center, resulting in the cleavage of one C–C bond and the formation of a new C–C bond. Finally, the remaining C–Ag bond donates its electrons to the rearranged carbocation, leading to the formation of the second C–C bond and the release of the final product.

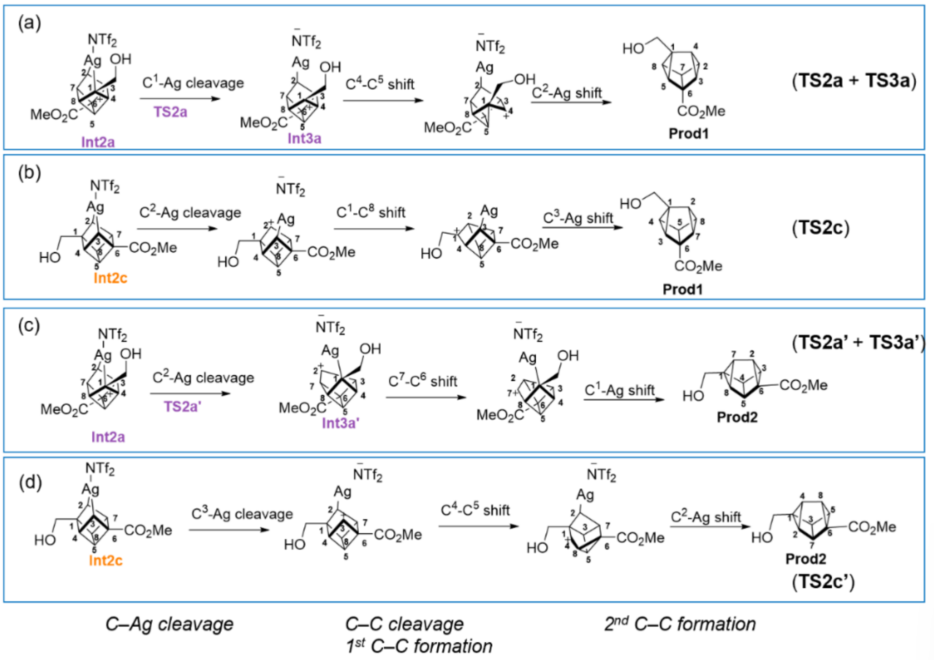

Figure 3. Schematic process of the formation of **Prod1** and **Prod2** through four possible pathways.

Regarding the nature of the rearrangement process, the high propensity for rearrangement of the cyclobutyl cation allows for the coupling of Ag–C bond heterolytic cleavage with the further bond cleavage or formation events. This tandem rearrangement demonstrates fascinating mechanistic diversity in terms of whether the process occurs concertedly or stepwise.

On the one hand, during the process initiated by OA into the C1–C2 bond, the Ag(III) intermediate, referred to as **Int2a**, converts into a carbocation intermediate, **Int3a**, through **TS2a**. During this reaction, the Ag–C1 bond is cleaved, resulting in a cationic C1 (Figure 3a). Int3a exhibits a bridged structure, where C5 is symmetrically positioned between C1 and C4. It readily undergoes further rearrangement, in which the C5–C4 bond cleaves, and the Ag–C2 bond is eliminated to form the C2–C4 bond, leading to the release of the final product, **Prod1**. Notably, Int3a has two adjacent C–C bonds near the C1 cationic center, namely C5–C4 and C5–C8. These two bonds are formally symmetric, although they differ in specific conformers based on the orientation of the hydroxyl group. During the IRC curve, the C5–C4 bond, which is cis- to the hydroxyl group, participates in the formation of the bridged carbocation. As there is no chiral ligand present, the conformer with the hydroxyl group cis- to the C5–C8 bond has an identical energy, resulting in the two bonds having an equal probability of migration. However, the migration of one of these two bonds will determine the enantioselectivity of the overall reaction once a chiral ligand is introduced. This preference will be further discussed in a later section.

On the other hand, the tandem rearrangement starting from the intermediate formed by OA into the C2–C3 bond, namely Int3c, is concerted. According to the intrinsic reaction coordinate (IRC) through **TS2c** (Figure 3b), all the necessary bond adjustments to achieve Prod1 occur successively. Starting from Int2c, the C2–Ag bond is partially cleaved, accompanied by a rapid shift of the C1–C8 bond towards the cationic C2, resulting in a flat region A on the IRC curve. This migration leads to partial carbocation character on the tertiary carbon C1. However, this carbocation is not an intermediate; it readily collapses once C1 approaches the C3–Ag bond, ultimately facilitating the formation of the second C–C bond and the release of Prod1.

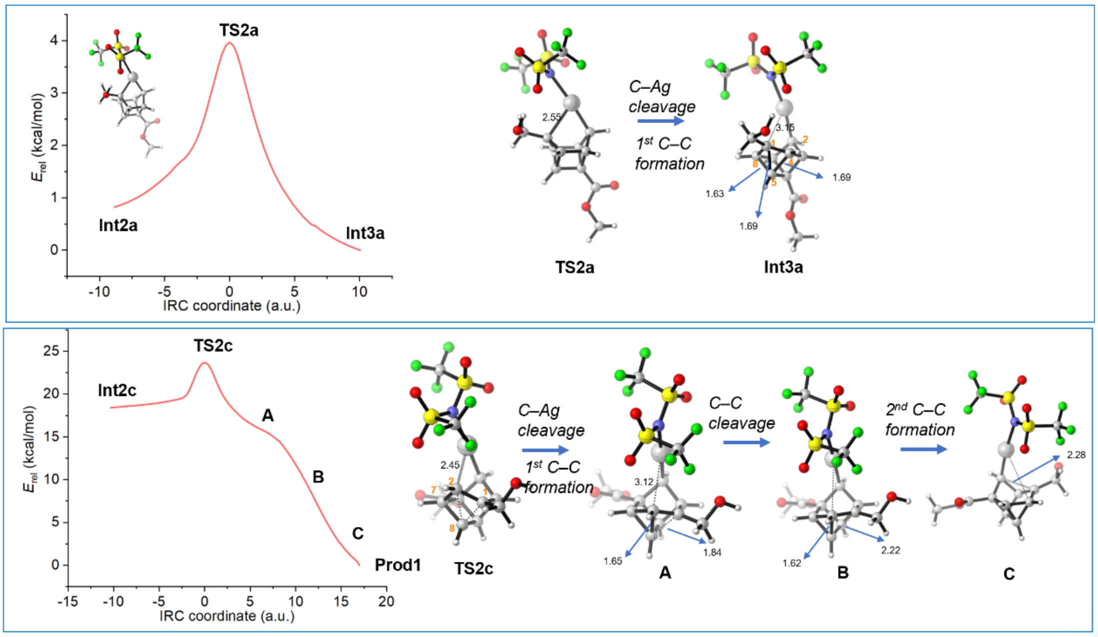

Figure 3. IRC curve and selected key geometries for (a) **TS2a** and (b) **TS2c**.

The dynamic behavior of the molecule on the reaction pathways is further studied using quasi-classical molecular dynamics simulations (Figure 4). A total of 80 trajectories were initiated from **TS2a**, and 55 trajectories were initiated from **TS2c**. The evolution of key bond lengths was recorded. Although **TS2a** results in a carbocation intermediate, the reaction is dynamically concerted, consistent with the very low rearrangement barrier through **TS3a**. Starting from **TS2a**, the C1–Ag cleavage event occurs rapidly with an average timing of 96.4 fs, followed by the formation of C1–C5 bond, resulting in the formation of the carbocation **Int3a**. However, the C4–C5 bond dissociates quickly, leading to additional rearrangement. The average timing for C4–C5 bond cleavage is 319 fs, while in some trajectories, this event occurs even earlier (~200 fs). A few tens of femtoseconds later, the second C–C bond formation event occurs. Although the IRC curve shows that C4–C5 participates in forming a bridged carbocation, both C4–C5 and C8–C5 migrate along the trajectories (C4–C5 migrates in 26 trajectories and C8–C5 migrates in 17 trajectories), leading to the formation of C4–C2 and C8–C2 bonds, respectively. The average durations for these two types of trajectories are quite similar (365 and 364 fs, respectively).

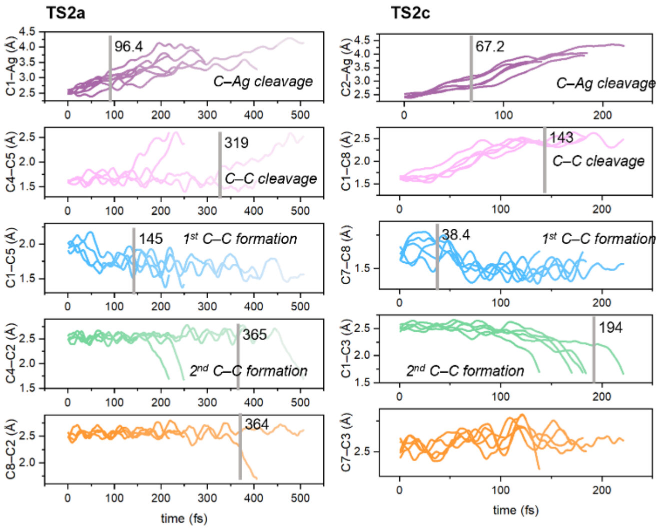

Figure 4. Evolution of key bond lengths along selected quasi-classical molecular dynamics trajectories initiated from **TS2a** and **TS2c**. The average timings for each bond cleavage or formation event are labelled beside gray vertical lines (in fs).

In the case of trajectories initiated by **TS2c**, all bond adjustment events occur much more rapidly. The formation of the C7–C8 bond takes place prior to the cleavage of the Ag–C bond, with average timings of 38.4 fs and 67.2 fs, respectively. Subsequently, the C1–C8 bond exclusively migrates at around 143 fs, followed by the formation of the second C–C bond within 194 fs. In summary, quasi-classical molecular dynamics simulations indicate that the tandem rearrangement through both **TS2a** and **TS2c** occurs in a dynamically concerted manner, albeit with different timings.

Metal Effect: Lam's reaction involves a novel oxidative addition (OA) into a non-polar C–C bond, and this step is achieved using Ag(I), a relatively uncommon transition metal catalyst. This section aims to explore the difference between Ag and other metals and clarify why Ag salt is the superior catalyst.

First, various potential metal catalysts were compared. Practical Au(I) and Cu(I) catalysts are typically used in combination with a soft ligand such as phosphine or nitrogen heterocyclic carbene (NHC). Therefore, three phosphine-ligated catalysts, namely $Ag(PMe_3)NTf_2$, $Au(PMe_3)NTf_2$, and $Cu(PMe_3)NTf_2$, were compared. Furthermore, the "bare" cationic Cu(I) catalyst, $CuNTf_2$, was also investigated (Figure 5).

The presence of the phosphine ligand PMe_3 significantly increases the reaction barrier for the Ag(I) catalyst. The complexation with the ester oxygen atom is endothermic for all three metals in the presence of PMe_3, indicating a decrease in Lewis acidity. The selectivity among the three types of C–C bonds during the OA step remains unchanged, but both the energy barrier and the barrier difference increase significantly. For both $Ag(PMe_3)NTf_2$ and $Cu(PMe_3)NTf_2$, the formation of the trivalent intermediate **Int2** is significantly disfavored, and its further rearrangement requires an even higher barrier (> 25 kcal/mol). For $Au(PMe_3)NTf_2$, the OA step becomes exothermic due to the stability of the Au(III) oxidation. Nonetheless, the reaction is limited by the high OA barrier.

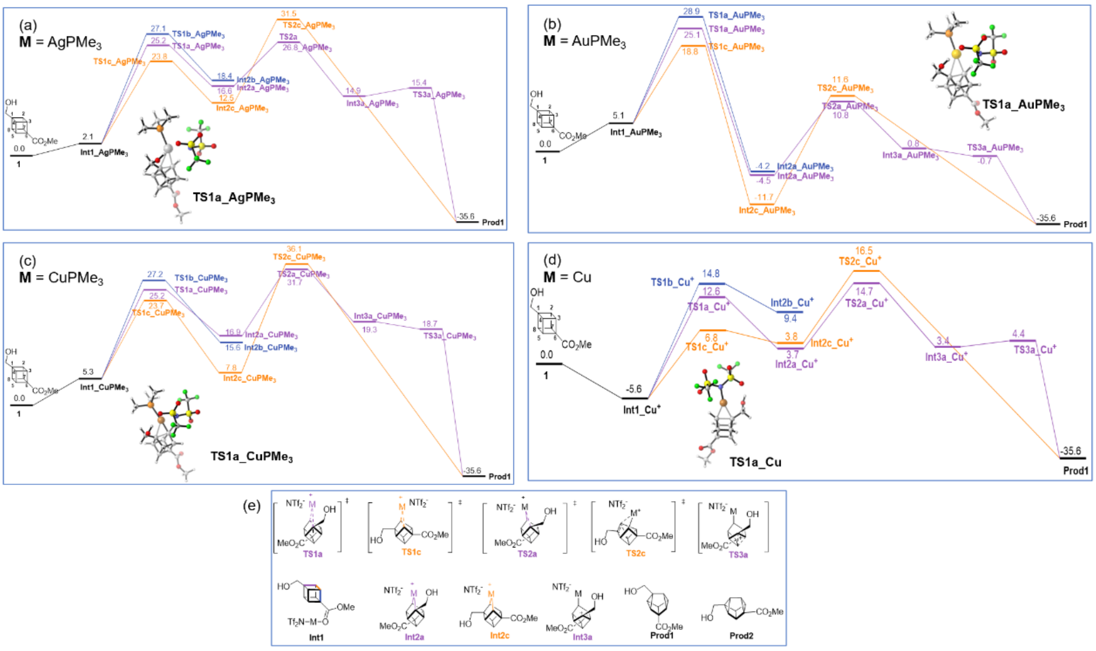

Figure 5. Gibbs free energy profile (kcal/mol) for the reaction using (a) Ag(PMe$_3$)NTf$_2$, (b) Au(PMe$_3$)NTf$_2$, (c) Cu(PMe$_3$)NTf$_2$ and (d) CuNTf$_2$ as catalyst. Structures of key compounds are shown in (e).

In the case of CuNTf$_2$, the shape of the Gibbs energy profile (Figure 5d) is more similar to that of AgNTf$_2$. The Cu–O complexation is exothermic, releasing -5.6 kcal/mol, and the subsequent formation of the C2–C3 bond requires a low barrier of 12.4 kcal/mol. The rate-determining step is the cleavage of the Cu–C bond, with an overall barrier of 20.3 kcal/mol, which is still significantly higher than that of AgNTf$_2$. Overall, the comparison of the three metals reveals that (1) ligands used in conjunction with practical Cu and Au catalysts may significantly impede the reaction; (2) while a bare cationic Cu(I) can facilitate rapid OA, the reaction efficiency is constrained by slow Cu–C bond cleavage. The superior behavior of the Ag catalyst may be attributed to two factors: (1) the easy accessibility of bare cationic Ag(I) salt, and (2) the smaller bond energy of the Ag(III)–C bond resulting from the larger atomic radius of Ag and the active Ag(III) oxidative state.

In addition to the group 11 elements, the reaction mediated by another important transition metal, Pd, was also investigated. When Pd(PMe$_3$)$_2$ was used as the catalyst (Figure 6), the OA towards the C–C bond requires a barrier of 20.6 ~ 24.4 kcal/mol. Interestingly, the selectivity differs slightly from that of the group 11 metals. The activation barriers for all three group 11 metals follow the order **TS1c** < **TS1a** < **TS1b**. Pd exhibits a preference for **TS1b** (23.4 kcal/mol) over **TS1c** (24.4 kcal/mol). This observation reflects the distinct electronic nature of the OA step, which will be discussed later. The formation of the OA product **Int2** with a Pd(II) oxidation state is significantly exothermic by -16.3~-25.4 kcal/mol. The strong stability of Pd(II) causes the following transformation to follow a different mechanism. The heterolytic cleavage of a Pd–C bond to form Pd(0) and a carbocation does not represent the minimum energy pathway. Instead, a dyatropic rearrangement is required, in which the positions of the C–Pd and C–C bonds exchange, resulting in another Pd(II) intermediate, **Int4_Pd**, which releases **Prod1** through a reductive elimination. The reaction efficiency is limited by the high barrier of the dyatropic rearrangement (> 35 kcal/mol), indicating that this reaction presents a challenge for Pd catalysts. Indeed, to the best of my knowledge, only a few sophisticatedly designed Pd catalysts have been successfully applied in the cubane rearrangement reaction.

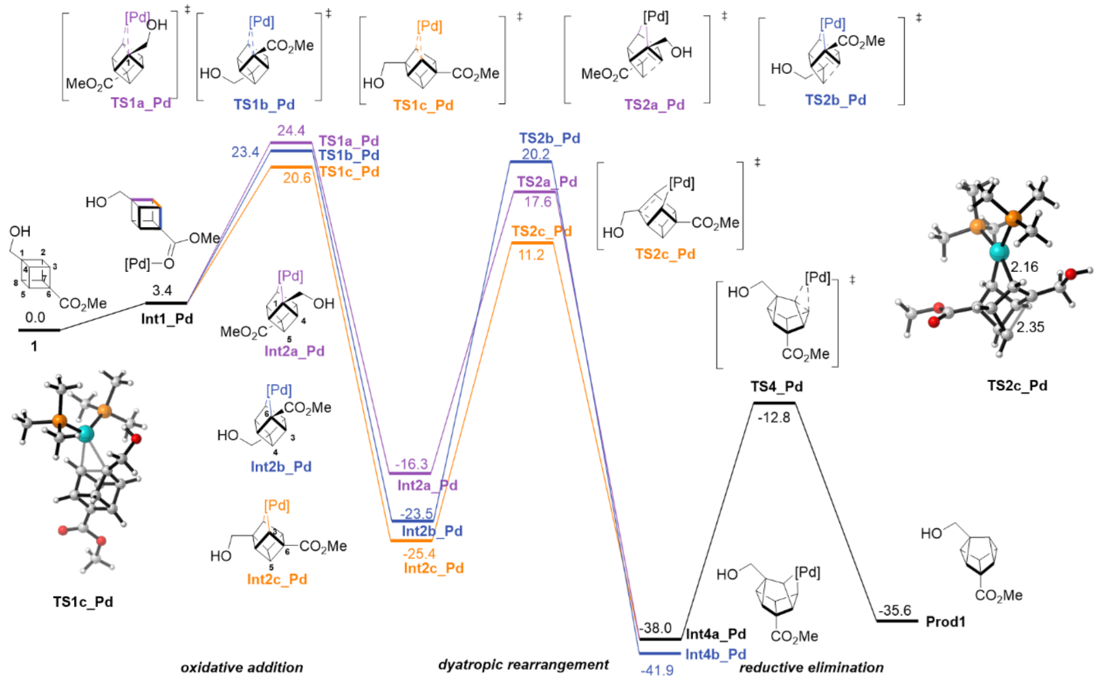

Figure 6. Gibbs free energy profile (kcal/mol) for the reaction using $Pd(PMe_3)_2$ as catalyst. [Pd] = $Pd(PMe_3)_2$.

Nature of the OA Step: In order to further clarify the electronic nature of the OA step promoted by Ag(I), natural bond orbital (NBO) and principle interactive orbital (PIO) analysis were performed (Figure 7).

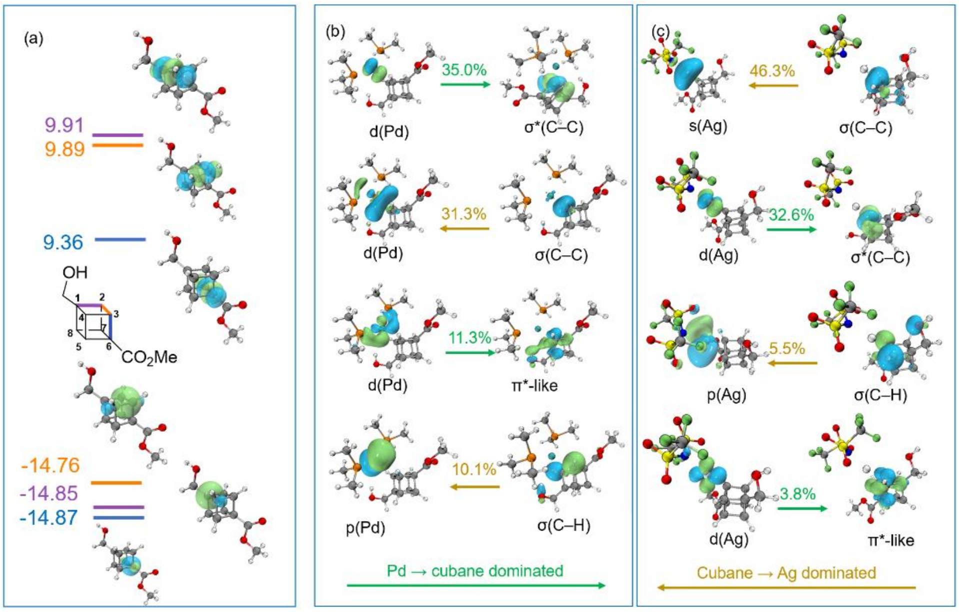

Figure 7. (a) Selected NBO levels for cubane substrate **1**. (b, c) PIO pairs and contributions between the metal and the substrate fragment for **TS1c_Pd** (b) and **TS1c** (c).

To assess the intrinsic reactivity of 1,6-disubstituted cubane **1**, NBOs for the σ- and σ*-orbitals of the three types of C–C bonds were analyzed. Due to the electron-withdrawing effect of the ester group on C6, the C3–C6 bond shows the lowest σ- and σ*- orbital levels. Instead, the C2–C3 bond exhibits the highest σ-orbital level (-14.76 eV), compared to -14.85 eV for C1–C2 and -14.87 eV for C3–C6, indicating that the C2–C3 bond has the strongest nucleophilicity in substrate **1**.

The orbital interaction between the metal and the substrate during the $AgNTf_2$ and $Pd(PMe_3)_2$ mediated OA process was compared through PIO analysis of **TS1c** and **TS1c_Pd**. For **TS1c_Pd** (Figure 7b), which corresponds to a typical OA process catalyzed by a noble metal, the d(Pd) to σ*(C–C) back-donation plays a significant role, contributing 35.0% to the overall interaction. The σ(C-C) to d(Pd) donation contributes to a smaller, but still significant, extent (31.3%). The remaining major contributors are the back-donation from d(Pd) to a π-like orbital (11.3%) and donation from σ(C-H) to p(Pd) (10.1%). Overall, the interaction between Pd and the substrate is dominated by metal-to-substrate back-donation (46.3%), while the substrate-to-metal donation interaction also plays a significant role (41.4%).

When $AgNTf_2$ is utilized as the catalyst (**TS1c**), the primary contributor to the metal-substrate orbital interaction is the donation from the σ(C–C) to the empty s(Ag) orbital (46.3%). The back-donation from d(Ag) to σ*(C–C) still exists but contributes significantly less (32.6%). The contributions of the other two types of interactions, namely (C–H) to p(Ag) donation and d(Ag) to -like orbital back-donation, are considerably lower, accounting for 3.8% and 5.5%, respectively. Overall, $AgNTf_2$ functions as an electrophile, with substrate-to-metal donation dominating (51.8% vs. 31.4% for back-donation). The electrophilic nature explains the preference for C2–C3 OA and the importance of a cationic metal catalyst that is as bare as possible.

***Ligand Engineering and Counteranion Effect*:** Although the electrophilic nature of the OA step stresses the significance of a bare cationic metal catalyst, a highly electrophilic catalyst may produce unexpected by-reactions for some Lewis acid-sensitive substrates. Furthermore, a bare cationic catalyst may experience stability issues. The goal of this section is to investigate the use of a ligand to stabilize the Ag(I) salt and minimize its Lewis acidity while retaining its high catalytic activity. A total of 25 ligands were computationally evaluated (Figure 8). The Lewis acidity is determined by the relative Gibbs free energy of Int1 beginning from separated **1** and $LAgNTf_2$, where L is the ligand investigated. Although both the OA and the rearrangement steps may be rate-determining, the OA step is taken as the starting point for ligand screening.

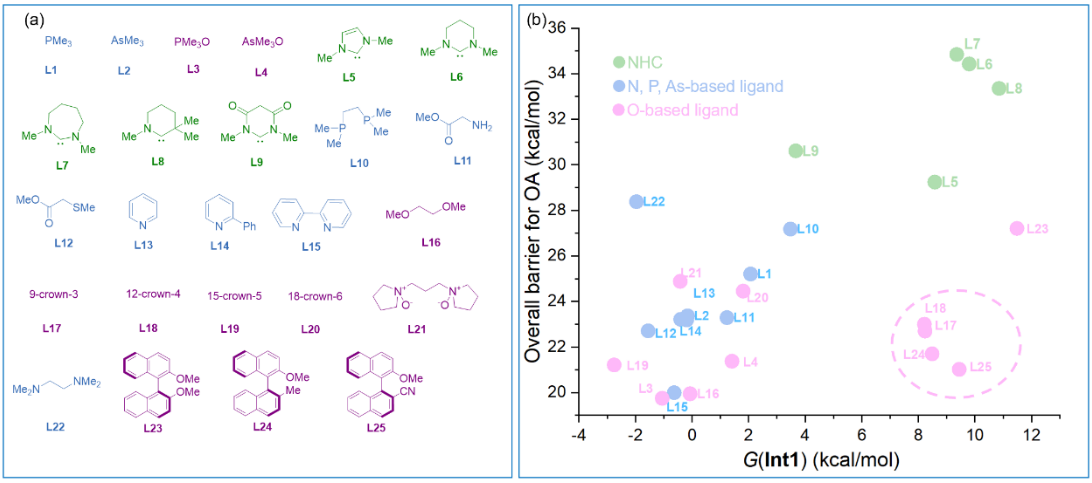

Figure 8. (a) Structures of the ligands investigated. (b) Overall OA barrier (through **TS1a**) and

relative Gibbs free energy of **Int1** in the presence of each ligand.

According to Figure 8b, a positive relationship between the OA barrier and *G*(**Int1**) can be observed. It is notable that a catalyst with low Lewis acidity generally exhibits a high barrier, except for some ether-based ligands (circled in Figure 8b). This observation aligns with the electrophilic nature of Ag(I)-mediated OA. Almost all ligands effectively reduce the Lewis acidity of silver, as evidenced by the decrease in *G*(**Int1**) from -8.3 kcal/mol for bare $AgNTf_2$. Consequently, NHCs, N, P, and As-based ligands significantly increase the OA barrier, rendering the reaction unfeasible.

The acidity-barrier relationship seems to be less restrictive for O-based ligands. Several ligands within the "ether circle," namely **L17**, **L28**, **L23** ~ **L25**, exhibit significantly lower OA barriers compared to what would be expected based on their corresponding *G*(**Int1**) values. The Lewis acidity of Ag in the presence of these ligands appears to be excessively suppressed, as indicated by their relatively high *G*(**Int1**) values (8~10 kcal/mol). Therefore, if the metal-substrate binding can be properly strengthened, there is hope that these ligands can lead to catalysts with both moderate Lewis acidity and high activity. Achieving this goal may involve fine-tuning of the counteranion.

With bare AgX salts as the catalyst (where X refers to the counteranion), the response of *G*(**Int1**) and *G*(**TS1a**) towards counteranions was evaluated (Table 1). Compared to NTf_2^-, only BF_4^- increases the binding strength. Hence, combining ether ligands with the BF_4^- counteranion may help balance the Lewis acidity and catalytic activity. It is worth noting that the phosphate counteranion, $P(OMe)_2O_2^-$, displays a significantly lower overall barrier among all the counteranions listed. This suggests that using a phosphate acid-derived silver salt could also be a candidate for further experimental optimization.

Table 1. The counteranions investigated, and the corresponding *G*(Int1), *G*(TS1a) and overall OA barrier (kcal/mol).

Counteranion	*G*(**Int1**)	*G*(**TS1a**)	Overall OA Barrier
NTf_2^-	-8.3	8.8	17.1
BF_4^-	-13.3	2.2	15.5
ClO_4^-	-3.5	11.4	14.9
NO_3^-	-3.4	13.0	16.4
OTf^-	-3.8	11.4	15.2
$P(OMe)_2O_2^-$	-3.7	8.3	12.0

Based on the aforementioned observations, the entire reaction was carried out using the **L24** ligand with the BF_4^- counteranion. This combined ligand-counteranion strategy effectively fine-tuned both the Lewis acidity and the OA barrier. The binding between Ag**L24**BF_4 and **1** is nearly thermal-neutral (0.6 kcal/mol), and the subsequent OA step requires a barrier of only 14.9 kcal/mol, which is even lower than that of the bare $AgNTf_2$ catalyst. Interestingly, in the presence of **L24**, the selectivity of the OA step is modified to favor the C1–C2 bond. Furthermore, the subsequent rearrangement occurs rapidly, with an overall barrier for the formation of **Prod1** of only 15.5 kcal/mol. Moreover, the product selectivity is also excellent, as evidenced by the high overall barrier for the formation of **Prod2** (19.6 kcal/mol through **TS2a'_L24BF$_4$**). Therefore, Ag**L24**BF_4 shows promise as a potential candidate for further optimization of the cubane rearrangement reaction.

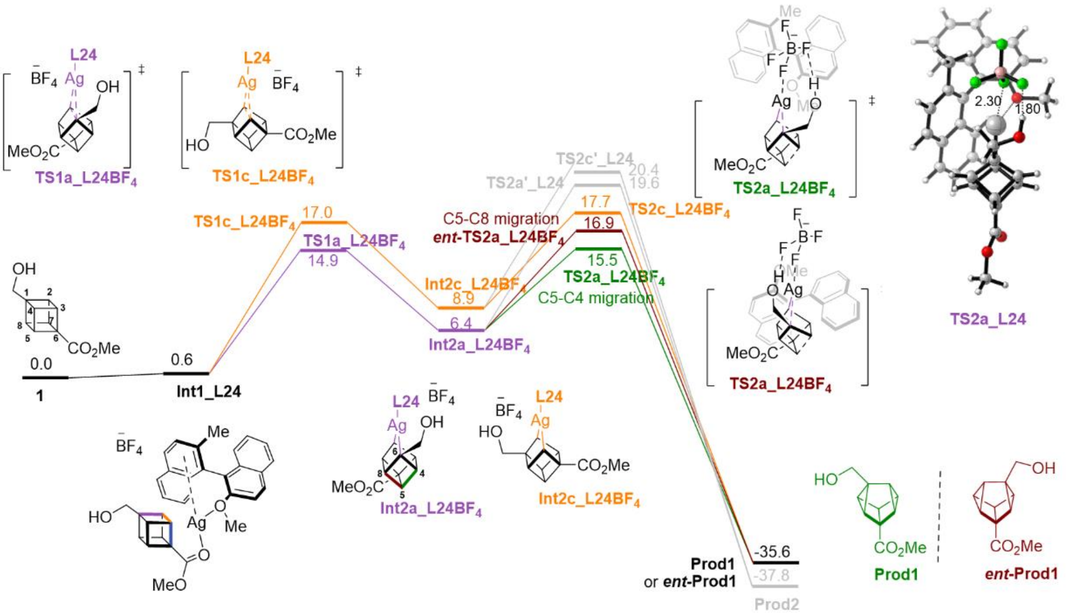

Figure 8. Gibbs free energy profile for the whole reaction using **L24** as the ligand and BF_4^- as the counteranion.

Post-TS Desymmetrization: In addition to its high activity, mild Lewis acidity, and excellent chemoselectivity, the use of **L24** as a ligand also offers an opportunity to achieve chiral synthesis. The reaction pathway through OA into the C1–C2 bond, which is the optimal pathway facilitated by Ag**L24**BF_4, results in an intermediate **Int2a** with a symmetric organic part. Migration of either the C5–C4 or C5–C8 bond can occur, resulting in the formation of **Prod1** or ***ent*-Prod1**, respectively (Figure 9a). However, when the chiral ligand **L24** is present, the migration probabilities of these two bonds are no longer equal. Due to the dynamically concerted nature of the rearrangement, the enantioselectivity is determined by the post-TS dynamical behavior of the molecule, leading to a post-TS desymmetrization process.

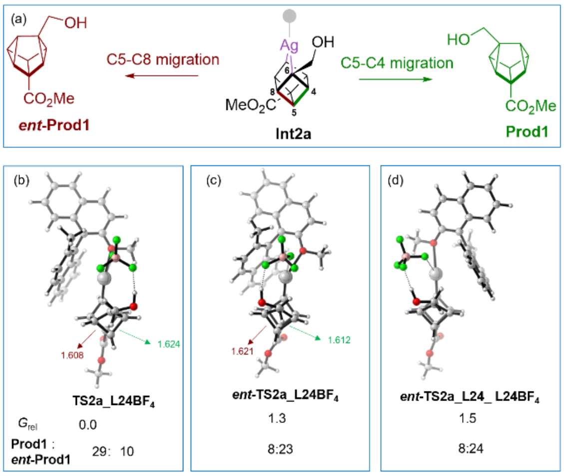

Figure 9. (a) The product structure resulted by desymmetrization process. (b~d) The geometry, relative free energy (kcal/mol), and the number of trajectories leading to two enantiomers for selected TSs. Bond lengths are in angstrom.

Quasi-molecular dynamics simulations were conducted to investigate three competitive conformers for the Ag–C bond cleavage/rearrangement TSs (Figure 9b-d). All TSs exhibit hydrogen bonding between BF_4^- and the hydroxymethyl group. Interestingly, the orientation of the hydroxyl group subtly influences the bond lengths of the two C–C bonds that may undergo migration. The C–C bond cis to the hydroxyl group consistently exhibits a longer bond length in all three TSs. Quasi-molecular dynamics trajectories further confirm that the C–C bond cis to the hydroxyl group has approximately three times of the probability of migration compared to the trans-C–C bond. This preference may arise from the electrostatic stabilization interaction between the partially negatively charged OH and the developing positive charge on the carbon atom.

The chirality of **L24** eliminates the degeneracy of the TSs with different orientations of the hydroxyl group. By averaging the contribution of all TSs according to their energies, the ratio of **Prod1** to ***ent*-Prod1** is determined to be 2.0:1. Although the enantioselectivity is low, the achievement of introducing enantioselectivity by a ligand remote from the rearrangement center and through post-TS manipulation is encouraging. By strategically incorporating bulky groups and enhancing the organization between the ligand and the counteranion in the TSs, the enantioselectivity could potentially be further improved.

Conclusions

In conclusion, this study utilized DFT, DLPNO-CCSD(T), and quasi-classical molecular dynamics calculations to investigate the Ag(I) salt-catalyzed cubane to cuneane rearrangement. The proposed mechanism was validated, demonstrating that Ag(I) initially undergoes OA into one of the three sets of C–C bonds, followed by heterolytic cleavage of one C–Ag bond and subsequent carbocation rearrangement. The selectivity of the reaction is co-controlled by the OA and rearrangement steps, leading to the formation of two isomeric products, **Prod1** and **Prod2**. The computational results align well with the experimental observations.

The OA step mediated by Ag(I) into a non-polar C–C bond is primarily electrophilic, relying on the donation from the substrate to the cationic Ag s-orbital. This finding underscores the importance of an electrophilic metal center in promoting the cubane to cuneane rearrangement reaction. A comparison of Cu(I), Ag(I), Au(I), and Pd(0) catalysts revealed that common Cu(I) and Au(I) catalysts are hindered by ligands associated with the metal center, which reduces their electrophilicity. In the case of "bare" $CuNTf_2$, the reaction is impeded by sluggish Cu–C bond cleavage. Hence, the superior performance of Ag(I) can be attributed to both the accessibility of bare Ag(I) salt and the relatively weak Ag–C bond.

While electrophilicity is crucial in the OA step, catalysts with high Lewis acidity may limit the reaction scope. To balance Lewis acidity and catalytic activity, a computational screening of ligands and counterions was performed. The chiral ether ligand, **L24**, in combination with BF_4^-, was suggested to form a superior catalytic system. This ligand combination both reduces the Lewis acidity of Ag(I) and lowers the overall energy barrier compared to the previously used $AgNTf_2$ catalyst. Additionally, the chemoselectivity is also suggested to be increased using this combination. Quasi-classical molecular dynamics simulations further indicate that **L24** could enable a desymmetrization process by influencing the migration probabilities of the C–C bonds. Although the achieved enantioselectivity with **L24** is moderate, the ability to introduce enantioselectivity through a ligand located remotely from the rearrangement center and by post-TS manipulation is encouraging. Further enhancement in enantioselectivity could be achieved by strategically incorporating bulky groups and strengthening the organization between the ligand and the counteranion in the transition states. Overall, these findings provide valuable insights into the Ag(I) salt-catalyzed cubane to cuneane rearrangement and offer a potential avenue for the development of efficient chiral synthesis strategies.

Acknowledgements

Computational resources and the Gaussian license were provided by Hangzhou Yanqu Information Technology Co., Ltd. The author acknowledges Wi Sugar, and all students in the Department of Chemistry, Tsinghua University, for their generous support, love, and encouragement towards the author.

Associated Content

- Data Availability Statements

The data underlying this study are available in the published article and its Supporting Information.

- Supporting Information Statement

Cartesian coordinates and energetics for all the species involved.

References

1. Rylander, P. N., *Organic syntheses with noble metal catalysts*. Elsevier: 2012; Vol. 28.
2. Bates, R., *Organic synthesis using transition metals*. John Wiley & Sons: 2012.
3. Tsuji, J., *Palladium in organic synthesis*. Springer Science & Business Media: 2005; Vol. 14.
4. Tsuji, J., *Organic synthesis with palladium compounds*. Springer Science & Business Media: 2012; Vol. 10.
5. Murahashi, S.-I., *Ruthenium in organic synthesis*. John Wiley & Sons: 2006.
6. Naota, T.; Takaya, H.; Murahashi, S.-I., Ruthenium-catalyzed reactions for organic synthesis. *Chemical reviews* **1998,** *98* (7), 2599-2660.
7. Tanaka, K., Rhodium catalysis in organic synthesis: methods and reactions. **2019**.
8. Oro, L. A.; Claver, C., *Iridium catalysts for organic reactions*. Springer Nature: 2021; Vol. 69.
9. Aneeja, T.; Neetha, M.; Afsina, C.; Anilkumar, G., Recent advances and perspectives in manganese-catalyzed C–H activation. *Catalysis Science & Technology* **2021,** *11* (2), 444-458.
10. Bauer, I.; Knölker, H.-J., Iron catalysis in organic synthesis. *Chemical reviews* **2015,** *115* (9), 3170-3387.
11. Plietker, B., *Iron catalysis in organic chemistry: reactions and applications*. John Wiley & Sons: 2008.
12. Hapke, M.; Hilt, G., *Cobalt catalysis in organic synthesis: Methods and reactions*. John Wiley & Sons: 2020.
13. Arora, V.; Narjinari, H.; Nandi, P. G.; Kumar, A., Recent advances in pincer–nickel catalyzed reactions. *Dalton Transactions* **2021,** *50* (10), 3394-3428.
14. Marin, M.; Rama, R. J.; Nicasio, M. C., Ni-Catalyzed Amination Reactions: An Overview. *The Chemical Record* **2016,** *16* (4), 1819-1832.
15. Shaughnessy, K. H.; Ciganek, E.; DeVasher, R. B., *Copper-catalyzed amination of aryl and alkenyl electrophiles*. John Wiley & Sons: 2017.
16. Chemler, S. R., Copper's contribution to amination catalysis. *Science* **2013,** *341* (6146), 624-626.
17. Zhang, Z.; Chen, P.; Liu, G., Copper-catalyzed radical relay in C (sp 3)–H functionalization.

Chemical Society Reviews **2022,** *51* (5), 1640-1658.

18. Yang, Y.; Gao, W.; Wang, Y.; Wang, X.; Cao, F.; Shi, T.; Wang, Z., Recent advances in copper promoted inert C (sp3)–H functionalization. *ACS Catalysis* **2021,** *11* (2), 967-984.

19. Michelet, V.; Toste, F. D., *Gold catalysis: an homogeneous approach*. World Scientific: 2014; Vol. 13.

20. Shahzad, S. A.; Sajid, M. A.; Khan, Z. A.; Canseco-Gonzalez, D., Gold catalysis in organic transformations: A review. *Synthetic Communications* **2017,** *47* (8), 735-755.

21. HARMATA, M., Silver in Organic Chemistry. **2010**.

22. Naodovic, M.; Yamamoto, H., Asymmetric silver-catalyzed reactions. *Chemical reviews* **2008,** *108* (8), 3132-3148.

23. Zheng, Q.-Z.; Jiao, N., Ag-catalyzed c–h/c–c bond functionalization. *Chemical Society Reviews* **2016,** *45* (16), 4590-4627.

24. Li, C.-J.; Bi, X., *Silver Catalysis in Organic Synthesis, 2 Volume Set*. John Wiley & Sons: 2019.

25. Yamamoto, Y., Silver-catalyzed Csp− H and Csp− Si bond transformations and related processes. *Chemical reviews* **2008,** *108* (8), 3199-3222.

26. Sekine, K.; Yamada, T., Silver-catalyzed carboxylation. *Chemical Society Reviews* **2016,** *45* (16), 4524-4532.

27. Eaton, P. E.; Cassar, L.; Halpern, J., Silver (I)-and palladium (II)-catalyzed isomerizations of cubane. Synthesis and characterization of cuneane. *Journal of the American Chemical Society* **1970,** *92* (21), 6366-6368.

28. Takebe, H.; Matsubara, S., Catalytic Asymmetric Synthesis of 2, 6-Disubstituted Cuneanes through Enantioselective Constitutional Isomerization of 1, 4-Disubstituted Cubanes. *European Journal of Organic Chemistry* **2022,** *2022* (37), e202200567.

29. Smith, E.; Jones, K. D.; O'Brien, L.; Argent, S. P.; Salome, C.; Lefebvre, Q.; Valery, A.; Böcü, M.; Newton, G. N.; Lam, H. W., Silver (I)-Catalyzed Synthesis of Cuneanes from Cubanes and their Investigation as Isosteres. *Journal of the American Chemical Society* **2023,** *145* (30), 16365-16373.

30. Nagasawa, S.; Fujiwara, K.; Maeyama, R.; Segawa, R.; Hirasawa, N.; Hirokawa, T.; Iwabuchi, Y., Selective Synthesis of 1, 3-Substituted Cuneanes: En Route to Potent Bioisosteres of m-Substituted Benzenes. **2023**.

31. Son, J.-Y.; Aikonen, S.; Morgan, N.; Harmata, A.; Sabatini, J.; Sausa, R.; Byrd, E.; Ess, D.; Paton, R.; Stephenson, C., Exploring Cuneanes as Benzene Isosteres and Energetic Materials: Scope and Mechanistic Investigations into Regioselective Rear-rangements from Cubanes. **2023**.

32. Frisch, M. J.; Trucks, G. W.; Schlegel, H. B.; Scuseria, G. E.; Robb, M. A.; Cheeseman, J. R.; Scalmani, G.; Barone, V.; Petersson, G. A.; Nakatsuji, H.; Li, X.; Caricato, M.; Marenich, A. V.; Bloino, J.; Janesko, B. G.; Gomperts, R.; Mennucci, B.; Hratchian, H. P.; Ortiz, J. V.; Izmaylov, A. F.; Sonnenberg, J. L.; Williams; Ding, F.; Lipparini, F.; Egidi, F.; Goings, J.; Peng, B.; Petrone, A.; Henderson, T.; Ranasinghe, D.; Zakrzewski, V. G.; Gao, J.; Rega, N.; Zheng, G.; Liang, W.; Hada, M.; Ehara, M.; Toyota, K.; Fukuda, R.; Hasegawa, J.; Ishida, M.; Nakajima, T.; Honda, Y.; Kitao, O.; Nakai, H.; Vreven, T.; Throssell, K.; Montgomery Jr., J. A.; Peralta, J. E.; Ogliaro, F.; Bearpark, M. J.; Heyd, J. J.; Brothers, E. N.; Kudin, K. N.; Staroverov, V. N.; Keith, T. A.; Kobayashi, R.; Normand, J.; Raghavachari, K.; Rendell, A. P.; Burant, J. C.; Iyengar, S. S.; Tomasi, J.; Cossi, M.; Millam, J. M.; Klene, M.; Adamo, C.; Cammi, R.; Ochterski, J. W.; Martin, R. L.; Morokuma, K.; Farkas, O.; Foresman, J. B.; Fox, D. J. *Gaussian 16 Rev. C.01*, Wallingford, CT, 2016.

33. Adamo, C.; Barone, V., Toward reliable density functional methods without adjustable parameters:

The PBE0 model. *The Journal of Chemical Physics* **1999,** *110* (13), 6158-6170.

34. Clark, T.; Chandrasekhar, J.; Spitznagel, G. W.; Schleyer, P. V. R., Efficient diffuse function-augmented basis sets for anion calculations. III. The 3-21+ G basis set for first-row elements, Li–F. *Journal of Computational Chemistry* **1983,** *4* (3), 294-301.

35. Ditchfield, R.; Hehre, W. J.; Pople, J. A., Self-consistent molecular-orbital methods. IX. An extended Gaussian-type basis for molecular-orbital studies of organic molecules. *The Journal of Chemical Physics* **1971,** *54* (2), 724-728.

36. Francl, M. M.; Pietro, W. J.; Hehre, W. J.; Binkley, J. S.; Gordon, M. S.; DeFrees, D. J.; Pople, J. A., Self-consistent molecular orbital methods. XXIII. A polarization-type basis set for second-row elements. *The Journal of Chemical Physics* **1982,** *77* (7), 3654-3665.

37. Gordon, M. S.; Binkley, J. S.; Pople, J. A.; Pietro, W. J.; Hehre, W. J., Self-consistent molecular-orbital methods. 22. Small split-valence basis sets for second-row elements. *Journal of the American Chemical Society* **1982,** *104* (10), 2797-2803.

38. Hehre, W. J.; Ditchfield, R.; Pople, J. A., Self—Consistent Molecular Orbital Methods. XII. Further Extensions of Gaussian—Type Basis Sets for Use in Molecular Orbital Studies of Organic Molecules. *The Journal of Chemical Physics* **2003,** *56* (5), 2257-2261.

39. Hariharan, P. C.; Pople, J. A., The influence of polarization functions on molecular orbital hydrogenation energies. *Theoretica chimica acta* **1973,** *28* (3), 213-222.

40. Grimme, S.; Antony, J.; Ehrlich, S.; Krieg, H., A consistent and accurate ab initio parametrization of density functional dispersion correction (DFT-D) for the 94 elements H-Pu. *The Journal of Chemical Physics* **2010,** *132* (15).

41. Marenich, A. V.; Cramer, C. J.; Truhlar, D. G., Universal solvation model based on solute electron density and on a continuum model of the solvent defined by the bulk dielectric constant and atomic surface tensions. *The Journal of Physical Chemistry B* **2009,** *113* (18), 6378-6396.

42. Guo, Y.; Riplinger, C.; Becker, U.; Liakos, D. G.; Minenkov, Y.; Cavallo, L.; Neese, F., Communication: An improved linear scaling perturbative triples correction for the domain based local pair-natural orbital based singles and doubles coupled cluster method [DLPNO-CCSD (T)]. *The Journal of chemical physics* **2018,** *148* (1).

43. Rappoport, D.; Furche, F., Property-optimized Gaussian basis sets for molecular response calculations. *The Journal of Chemical Physics* **2010,** *133* (13).

44. Weigend, F.; Ahlrichs, R., Balanced basis sets of split valence, triple zeta valence and quadruple zeta valence quality for H to Rn: Design and assessment of accuracy. *Physical Chemistry Chemical Physics* **2005,** *7* (18), 3297-3305.

45. Neese, F.; Wennmohs, F.; Becker, U.; Riplinger, C., The ORCA quantum chemistry program package. *The Journal of chemical physics* **2020,** *152* (22).

46. Ho, J.; Klamt, A.; Coote, M. L., Comment on the Correct Use of Continuum Solvent Models. *The Journal of Physical Chemistry A* **2010,** *114* (51), 13442-13444.

47. Zhao, Y.; Schultz, N. E.; Truhlar, D. G., Design of Density Functionals by Combining the Method of Constraint Satisfaction with Parametrization for Thermochemistry, Thermochemical Kinetics, and Noncovalent Interactions. *Journal of Chemical Theory and Computation* **2006,** *2* (2), 364-382.

48. Legault, C., CYLview, 1.0 b, Université de Sherbrooke. *Sherbrooke, QC: http://www. cylview. org* **2009**.

49. Humphrey, W.; Dalke, A.; Schulten, K., VMD: visual molecular dynamics. *Journal of molecular graphics* **1996,** *14* (1), 33-38.

50. Singleton, D. A.; Hang, C.; Szymanski, M. J.; Greenwald, E. E., A New Form of Kinetic Isotope Effect. Dynamic Effects on Isotopic Selectivity and Regioselectivity. *Journal of the American Chemical Society* **2003,** *125* (5), 1176-1177.